ARTICLES
https://doi.org/10.1038/s41561-020-0586-1

nature geoscience

Widespread biomass burning smoke throughout the remote troposphere

G. P. Schill[1,2]✉, K. D. Froyd[1,2], H. Bian[3,4], A. Kupc[1,2,5], C. Williamson[1,2], C. A. Brock[1], E. Ray[1,2], R. S. Hornbrook[6], A. J. Hills[6], E. C. Apel[6], M. Chin[4], P. R. Colarco[4] and D. M. Murphy[1]

Biomass burning emits ~34–41 Tg yr^{-1} of smoke aerosol to the atmosphere. Biomass burning aerosol directly influences the Earth's climate by attenuation of solar and terrestrial radiation; however, its abundance and distribution on a global scale are poorly constrained, particularly after plumes dilute into the background remote troposphere and are subject to removal by clouds and precipitation. Here we report global-scale, airborne measurements of biomass burning aerosol in the remote troposphere. Measurements were taken during four series of seasonal flights over the Pacific and Atlantic Ocean basins, each with near pole-to-pole latitude coverage. We find that biomass burning particles in the remote troposphere are dilute but ubiquitous, accounting for one-quarter of the accumulation-mode aerosol number and one-fifth of the aerosol mass. Comparing our observations with a high-resolution global aerosol model, we find that the model overestimates biomass burning aerosol mass in the remote troposphere with a mean bias of >400%, largely due to insufficient wet removal by in-cloud precipitation. After updating the model's aerosol removal scheme we find that, on a global scale, dilute smoke contributes as much as denser plumes to biomass burning's scattering and absorption effects on the Earth's radiation field.

Wildfires and open burning emit ~2.8–4.9 Tg yr^{-1} of black carbon (BC) aerosol and ~31–36 Tg yr^{-1} of primary organic aerosol[1,2]. These estimates correspond to ~40–59% of global BC and ~60–85% of global primary organic aerosol emissions. In a future climate, some regions are expected to be both warmer and drier, causing the frequency and intensity of fires to increase[3]. In areas like the western United States, there is evidence that fire intensity and frequency are already increasing[4,5]. Thus, biomass burning aerosol has an increasing potential to affect the Earth's climate system via both direct (light-attenuating) and indirect (cloud modification) aerosol effects.

Evidence suggests that the background atmosphere may be greatly influenced by biomass burning. For example, in situ observations have shown that one-third of the background particles in the North American free troposphere originate from biomass burning[6]. Filter-based measurements have shown that biomass burning accounts for 20–30% of the annually averaged mass concentration of atmospheric particles with diameters <2.5 µm in the United States[7]. Furthermore, it is known that smoke plumes are transported thousands of kilometres away from their sources[8–10] in both the boundary layer[11] and upper troposphere/lower stratosphere[12,13], where they are eventually removed or dissipate into background air. Despite this evidence, in situ quantitative measurements of biomass burning aerosol in the global remote troposphere are largely missing[14].

Without in situ observational constraints, global climate models rely heavily on satellite remote sensing to constrain biomass burning aerosol abundance. The most useful of these measurements resolve the aerosol vertical distribution, which can affect both the magnitude and sign of its radiative effects[15]. Unfortunately, satellite remote-sensing techniques that determine aerosol vertical distribution, such as the Cloud-Aerosol Lidar with Orthogonal Polarization (CALIOP) or the Multiangle Imaging SpectroRadiometer (MISR), are severely limited in the remote troposphere because background aerosol concentrations are very often below their limits of detection[16,17]. They also report over a small swathe once or twice daily and cannot observe through clouds. Undetected aerosol can account for >40% of the aerosol mass, causing a globally averaged bias in aerosol optical depth (AOD) of −25% or greater[17]. Thus, in situ aircraft measurements capable of sampling low concentrations of biomass burning aerosol are vital to the validation of global climate models and estimation of the present and future climatic impact of biomass burning aerosol.

Global-scale aircraft measurements of biomass burning aerosol

To provide constraints on biomass burning abundance and distribution in remote regions of the troposphere, we performed global-scale measurements of aerosol composition and size distributions during four seasonal flight campaigns between 2016 and 2018, as part of NASA's Atmospheric Tomography Missions (ATom). ATom targeted the remote troposphere, flying over the Pacific and Atlantic Oceans from ~85° S to ~82° N and taking near-continuous altitude profiles from ~0.18 to ~12 km (Supplementary Fig. 1). Biomass burning particles were detected using the instrument Particle Analysis by Laser Mass Spectrometry (PALMS)[18–20], which detects single particles of diameter between ~0.15 and ~5 µm. PALMS particle type classification errors are typically <5% (ref. [21]). For biomass burning particles, this is corroborated by calculation of particle number fractions inside biomass burning plumes: >90% of particles in smoke plumes, as defined by elevated acetonitrile and CO concentrations, were identified as biomass burning[6], but few smoke particles were identified in air with low biomass burning influence[22].

[1]Chemical Sciences Laboratory, NOAA Earth System Research Laboratories, Boulder, CO, USA. [2]Cooperative Institute for Research in Environmental Sciences, University of Colorado, Boulder, CO, USA. [3]Joint Center for Environmental Technology University of Maryland Baltimore County, Baltimore, MD, USA. [4]Laboratory for Atmospheres, NASA Goddard Space Flight Center, Greenbelt, MD, USA. [5]Faculty of Physics, Aerosol Physics and Environmental Physics, University of Vienna, Vienna, Austria. [6]Atmospheric Chemistry Observations & Modeling Laboratory, National Center for Atmospheric Research, Boulder, CO, USA. ✉e-mail: gregory.schill@noaa.gov

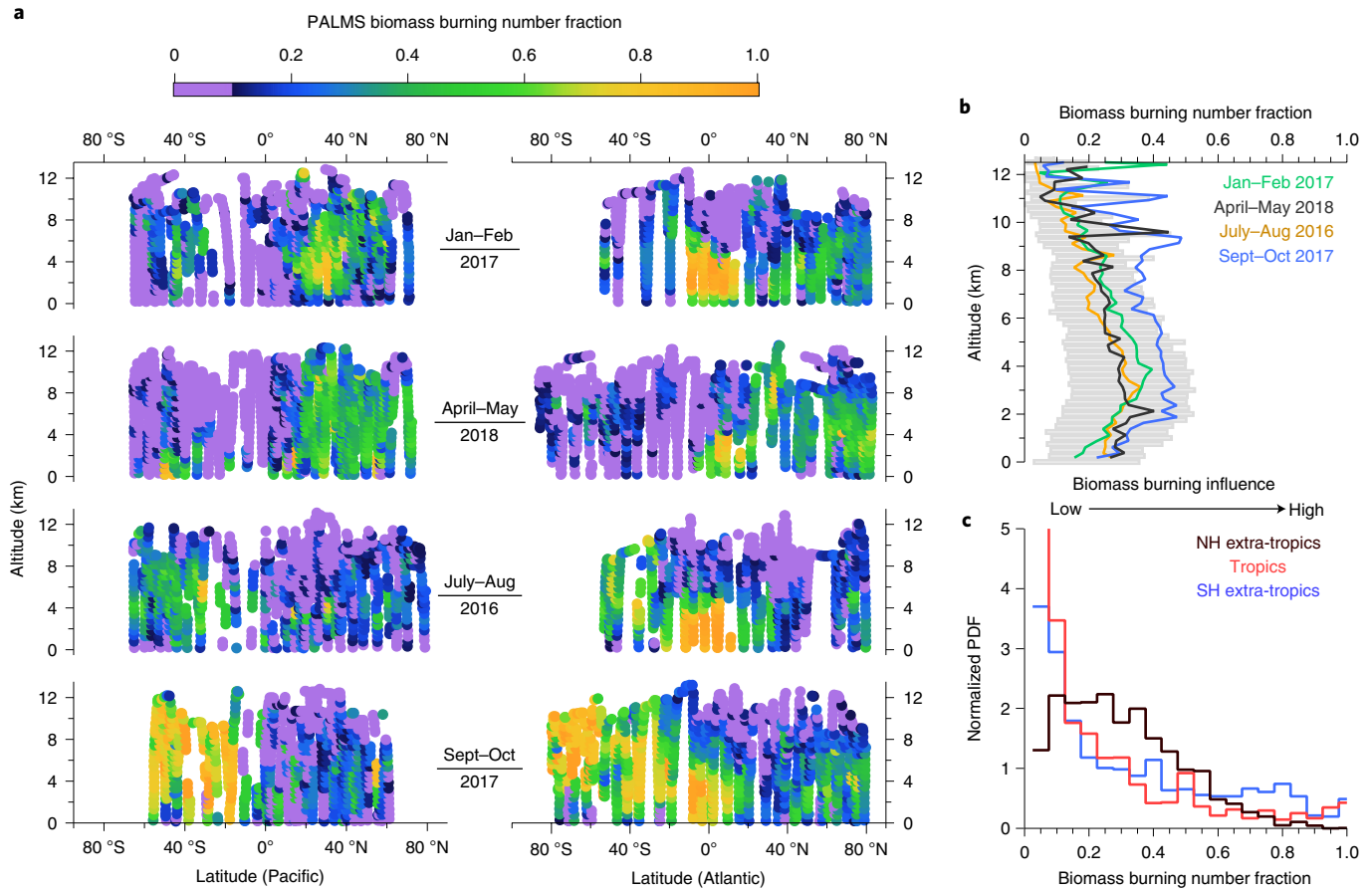

Fig. 1 | The influence of biomass burning on aerosol in the remote troposphere. a–c, PALMS biomass burning number fractions shown as altitude/latitude curtain plots, split by season and ocean basin (**a**), seasonal average vertical profiles (coloured lines) and mission-wide IQRs (grey boxes) (**b**) and mission-wide normalized probability density functions (PDFs), split into three latitude bins (**c**). See Supplementary Table 1 for region definitions. NH, Northern Hemisphere; SH, Southern Hemisphere.

Historically, airborne single-particle mass spectrometry instruments were limited to qualitative or relative measurements of particle abundance. Here, absolute number fractions and mass concentrations are derived using a new method[21] that pairs PALMS to an independent suite of optical particle counters that size aerosols quantitatively. To ensure statistically significant counts, quantitative size distributions are split into four bins and particle concentration data are aggregated by time (3 min). For a 3 min sampling period, the estimated statistical errors due to PALMS particle sampling and identification are ~30% at a mass concentration of 0.01 μg m^{-3}, decreasing to ~10% at 0.1 μg m^{-3} (ref. [21]).

From these global-scale in situ measurements, we find that biomass burning particles are ubiquitous in the remote troposphere. Here, we define the remote troposphere as all of the ATom measurements excluding take-offs, final approaches and low passes over continental land masses (Supplementary Fig. 1). Transported biomass burning plumes, such as the air off the west coast of Africa (Fig. 1a), were not filtered out. Biomass burning influenced (that is, biomass burning number fractions were >0.1) over two-thirds of air masses in ATom (Fig. 1a) and, on average, 27% of the accumulation-mode (particles of diameter >100 nm) aerosol particles in the remote troposphere originated in a fire. Furthermore, although <20% of all fire plumes are injected above the atmospheric boundary layer[23,24], biomass burning influences aerosol number throughout the remote tropospheric column (Fig. 1b). Between 2 and 8 km in altitude, biomass burning aerosol comprised 11–46% (interquartile range, IQR) of the accumulation-mode aerosol number. Number fractions at higher altitudes (8–12 km) were smaller but still non-trivial (4–30%), indicating that these surface-emitted particles are transported vertically, consistent with observations over the North Atlantic[12,13]. Biomass burning mass concentrations are consistent with the ubiquity observed in particle number (Supplementary Fig. 2). The range of biomass burning aerosol mass during ATom was 0.05–0.22 μg m^{-3} (IQR), with a mean mass concentration of 0.30 μg m^{-3}. Fractionally, biomass burning accounts for 6–30% (IQR) of the total aerosol mass in the remote troposphere, with a mean contribution of 21%.

The level of biomass burning influence in the remote troposphere ranges from negligible in pristine regions to dominant in well-defined plumes directly transported from burning sources; however, a majority of the influence during ATom was in an intermediate range where biomass burning aerosol comprised 10–50% of the accumulation-mode number (Fig. 1c). For example, while African biomass burning routinely emits widespread smoke plumes into the tropical Atlantic, integrating the normalized probability density function between biomass burning number fractions 0.5 and 1.0 shows that <13% of the air sampled in the remote tropics is dominated by biomass burning. Similarly, the Northern Hemisphere extra-tropics are pervasively influenced by biomass burning; however, the air was dominated by biomass burning only 13% of the time. In the clean Southern Hemisphere extra-tropics, sporadic biomass burning events can easily dominate over the low background of other particle types. Yet here, biomass burning dominated the

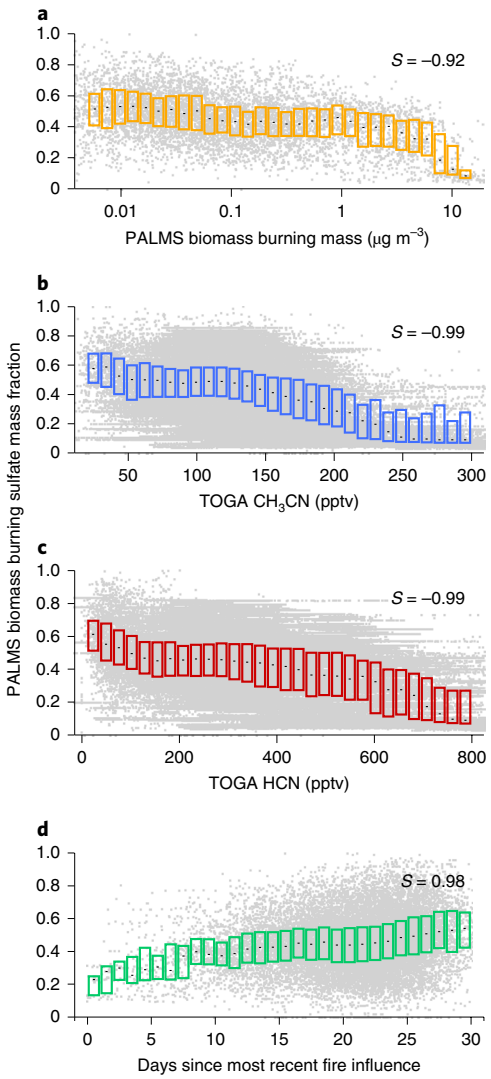

Fig. 2 | Sulfate mass fraction of biomass burning particles versus smoke markers. a–d, Sulfate mass fraction versus PALMS biomass burning mass (**a**), CH_3CN (**b**), HCN (**c**) and recent fire influence calculated from back trajectories (**d**). Raw data are shown as light grey dots, median values as horizontal black markers and IQRs as coloured boxes. For each plot, Spearman's Rho (*S*), a non-parametric measure of rank correlation, is provided for median values. All |*S*| are > 0.9, indicating monotonic relationships. pptv, parts per trillion by volume. Additional data shown in **b** and **c** are derived from the Studies of Emissions, Atmospheric Composition, Clouds and Climate Coupling by Regional Surveys mission[41], and extend this analysis to include fresh smoke plumes over the continental United States.

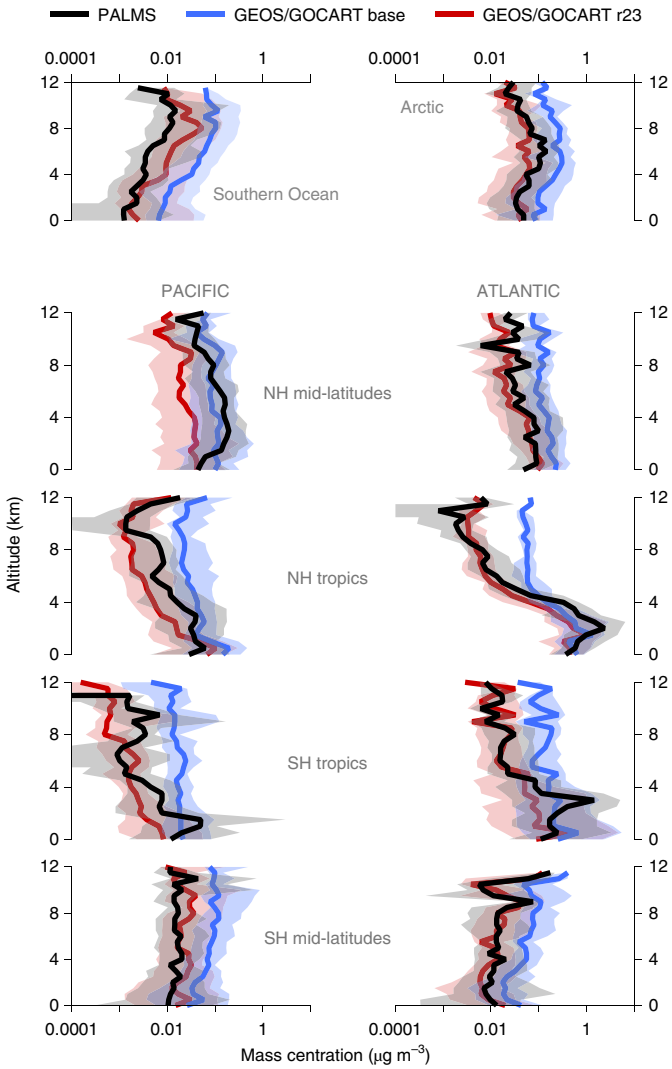

Fig. 3 | Global-scale model–measurement comparisons of biomass burning aerosol for all ATom campaigns. Lines correspond to median values, and shadings to the IQR of the values. Agreement of GEOS/GOCART aerosol with measurements (black) was improved over the base simulation case (blue) by adopting a more realistic aerosol wet removal scheme (red, see Supplementary Table 2). Vertical profiles are split into different latitude bins, and also by ocean basin outside of polar regions. Latitude bins were chosen from changes in east–west surface wind direction, temperature, water vapour and relative humidity, and the distribution of biomass burning gas-phase and aerosol tracers (Supplementary Table 1).

aerosol number only 25% of the time. This analysis suggests that, while biomass burning is ubiquitous, it is mostly due to a pervasive, dilute background rather than concentrated plumes.

Generally, fresh biomass burning particles are >90% carbonaceous material[25]; however, as biomass burning particles age, they can accumulate secondary sulfate mass[26] from condensation of gaseous sulfuric acid that is present in the background atmosphere. To assess the extent of dilution and ageing, we determined the organic and sulfate mass fractions of individual biomass burning particles[21] (Fig. 2). In ATom, we find that biomass burning sulfate mass fractions show near-monotonic increases with the decline in various smoke indicators (Fig. 2a–c). This is consistent with sulfate accumulation following ageing, loss of organic species or both. Biomass burning sulfate mass fraction also increases with the average number of days since crossing a fire plume, as indicated by back-trajectory analysis (Fig. 2d). Sulfate mass fractions in biomass burning particles varied from 0.35 to 0.55 (IQR). Thus, most of the ubiquitous smoke in the remote troposphere has indeed been diluted from plume conditions (by gas-phase biomass burning tracers) and is generally ≥1 week in age.

Model–observation comparisons and sensitivity tests

To assess the climatic relevance of this persistent, aged smoke in the remote troposphere, we conducted a detailed comparison of PALMS ATom biomass burning abundance with a high-resolution (~50 km horizontal resolution with 72 vertical layers) global atmospheric model, the Goddard Earth Observing System model v.5 (GEOS).

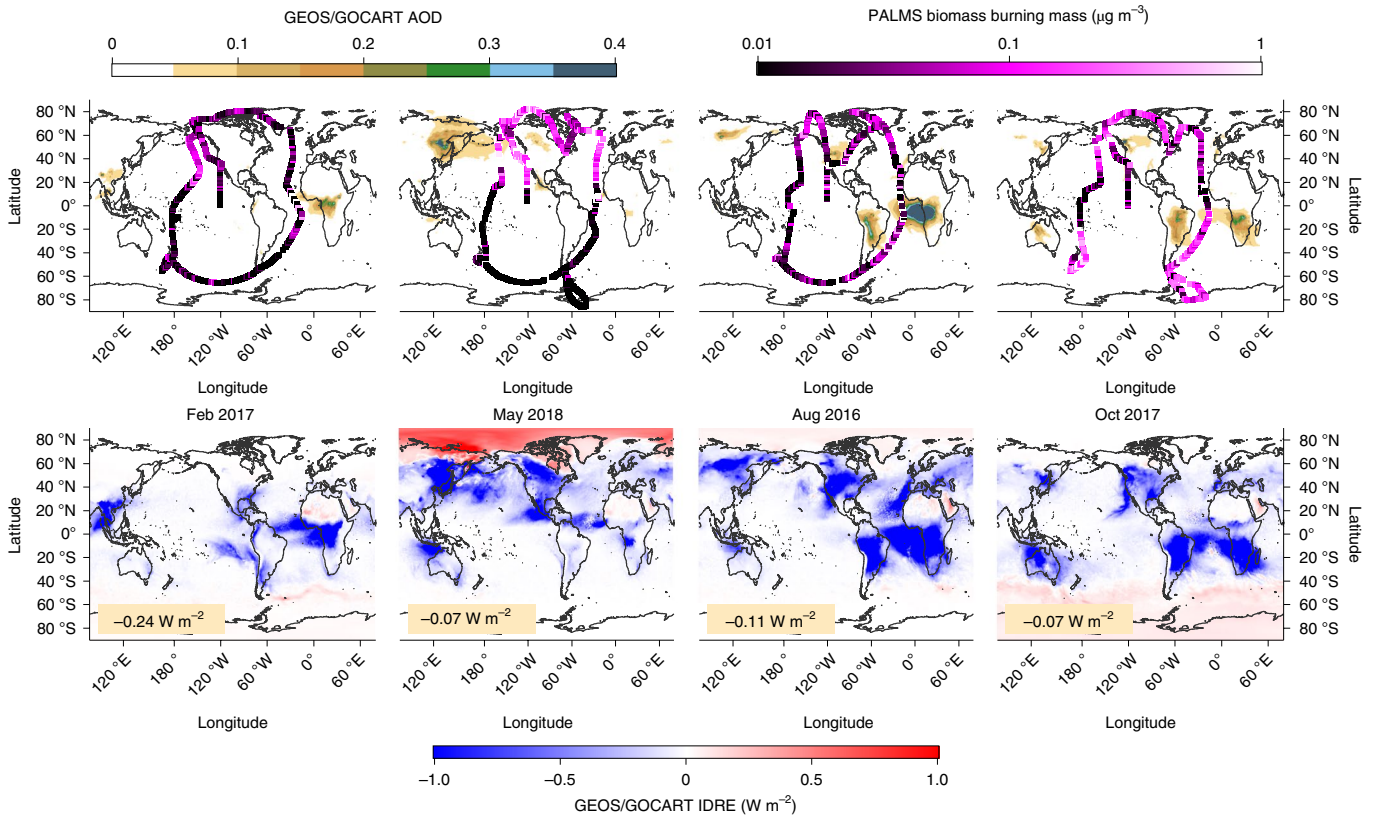

Fig. 4 | GEOS/GOCART r23 biomass burning-only, clear-sky AOD for primary ATom campaign months. The colour scale (top) emphasizes areas where biomass burning-only AOD > 0.05. Overlaid on the AOD plots are the ATom flight tracks, coloured by PALMS biomass burning mass concentration. The corresponding all-sky IDRE for biomass burning aerosol is also shown (bottom), with globally averaged values in the bottom left hand corner of each plot.

The Goddard Chemistry, Aerosol, Radiation, and Transport (GOCART) aerosol module[27–29] was implemented in GEOS, and the Quick Fire Emissions Dataset (QFED)[30] was used for biomass burning emissions. Simulated biomass burning aerosol abundance was determined using a fire emissions on–minus–off approach. A direct comparison to the ATom measurements was ensured by 'flying' a virtual aircraft through the model domain along the same spatiotemporal coordinates as the ATom flights. We assume that the net flux of organic mass (from condensation and evaporation) in aged biomass burning particles is zero[31]; under this assumption, the PALMS-measured biomass burning organic-only mass provides a straightforward comparison to biomass burning mass simulated by the model.

The default GEOS/GOCART run (base case) overestimates biomass burning abundance compared to the observations, with a mean bias of +430% (Fig. 3). The largest overestimations are at high altitudes and high latitudes, where the model median values are often greater than the 75th percentile of the observations and the mean bias increases to +510–800%. Better agreement nearer to biomass burning sources is expected, since QFED is a top-down emissions inventory that, when implemented in GEOS/GOCART, performs well against remotely sensed and ground-based measurements of AOD[32,33]. Because transport to high altitudes and latitudes is associated with deep convection and processing by cold-clouds, precipitation-related aerosol losses (wet removal processes) are probably underestimated in the model. Other global modelling studies observed a similar disparity with primary aerosol using default wet removal schemes[34–36], suggesting that poor predictive capabilities of biomass burning aerosol in the remote atmosphere may be common to many aerosol models that are unconstrained by measurements.

To assess the relative roles of the simulated biomass burning aerosol emission and removal processes, we ran 12 sensitivity tests using different combinations of emissions datasets, hydrophobic-to-hydrophilic ageing of organic aerosol, wet removal in cold-clouds (temperature $T < 258$ K) and removal of hydrophobic particles in large-scale and convective clouds (Supplementary Table 2). The best test run was chosen to minimize both mean log bias and centred root mean squared log error (CRMSLE) in biomass burning aerosol mass, while also being physically consistent with known atmospheric processes. As expected, both mean log bias and CRMSLE were more sensitive to wet removal processes than ageing time scales (r13) and emissions datasets (r15). In the best model run (r23, Supplementary Fig. 4), two removal pathways were added to the base case for BC and organic carbon: (1) half of all hydrophobic particles were removed from both convective and large-scale clouds following a first-order loss rate, and (2) half of both hydrophobic and hydrophilic particles were removed from cold-clouds following a first-order loss rate (Supplementary Table 2). Updating wet removal processes per sensitivity run r23 reproduces both the magnitude and shape of the in situ vertical profiles (Fig. 3 and Supplementary Fig. 3), suggesting that hydrophobic aerosol can be removed in-cloud via impaction and that wet removal parameterizations should be applied more deeply into the mixed-phase cloud regime.

Biomass burning AOD and direct radiative effect. Despite its ubiquity, biomass burning aerosol mass in the remote troposphere is typically too dilute (IQR = 0.05–0.22 μg m^{-3}) for detection by satellite remote sensors, which provide the only continuous, near-global observations of AOD. The total AOD limit of detection for satellite remote sensors that can differentiate particle types, such as CALIOP and MISR, is ~0.05 (refs. [16,17,37]). The ATom flight tracks are primarily in remote regions of the troposphere where the biomass burning,

clear-sky AOD in the model is <0.05 (Fig. 4, top row). Thus, a validated global aerosol model is needed to assess the climatic impact of dilute smoke (biomass burning AOD < 0.05) in the remote troposphere. To determine the contribution of dilute smoke to the total biomass burning-only AOD, we summed model grid cells with biomass burning AOD < 0.05 over the entire globe (with area normalization) and divided by the total biomass burning-only AOD. AOD < 0.05 was chosen because it corresponds to the detection limit of remotely sensed products. It is also conservative; biomass burning plumes have previously been defined with remotely sensed data using an AOD threshold of 0.10–0.15 (ref. [32]). For the months shown in Fig. 4, the average contribution of this remote, aged smoke to the total biomass burning AOD ranged from 23 to 50% (mean, 40%). Increasing the limit to model grid cells with AOD < 0.1 (Supplementary Fig. 5) raised these contributions to 32 and 67% (mean 54%). Thus, dilute smoke in the remote troposphere is often below satellite AOD limits of detection but can contribute up to half of the total biomass burning-only AOD.

To investigate the contribution of pervasive, aged smoke to the atmospheric radiation balance, we also used the updated model to calculate the biomass burning-only, all-sky instantaneous direct radiative effect (IDRE; Fig. 4, bottom row), a measure of aerosol scattering and absorption effects on the Earth's radiation field. Globally averaged, biomass burning particles exhibit a negative IDRE (−0.24 to −0.07 W m^{-2}; Fig. 4). Regionally, biomass burning aerosol can warm the atmosphere over areas of high albedo, including persistent clouds, deserts and snow or ice (Fig. 4). This warming, however, may be modulated by considering 'rapid adjustments' (not included here)[38], where absorbing aerosol can change atmospheric heating rates, stability and near-cloud relative humidity[39]. Furthermore, in regions like the cloudy South Atlantic Ocean, the sign of biomass burning aerosol's IDRE will depend on the model's horizontal resolution and prescribed aerosol single-scattering albedo[40]. Like AOD, areas of fresh fires dominate large values of the IDRE; however, the remote troposphere is filled with many small, non-zero contributions to total IDRE. Similar to AOD, these contributions amount to a large fraction of the global biomass burning-only IDRE. For the ATom deployment months, the monthly averaged contribution of dilute smoke to the biomass burning-only, all-sky IDRE ranges from 35 to 57% (mean, 44%). Changing the limit to AOD <0.1, these contributions increase to 48 and 74% (mean 63%). Thus, while air in the remote troposphere does not contain large biomass burning mass concentrations, dilute and aged smoke is so pervasive that it, globally averaged, contributes approximately half of the total AOD and IDRE from all biomass burning.

Online content

Any methods, additional references, Nature Research reporting summaries, source data, extended data, supplementary information, acknowledgements, peer review information; details of author contributions and competing interests; and statements of data and code availability are available at https://doi.org/10.1038/s41561-020-0586-1.

Received: 20 September 2019; Accepted: 28 April 2020;
Published online: 1 June 2020

References

1. Bond, T. C. et al. Bounding the role of black carbon in the climate system: a scientific assessment. *J. Geophys. Res. Atmos.* **118**, 5380–5552 (2013).
2. Andreae, M. O. Emission of trace gases and aerosols from biomass burning—an updated assessment. *Atmos. Chem. Phys.* **19**, 8523–8546 (2019).
3. Bowman, D. M. J. S. et al. Fire in the Earth System. *Science* **324**, 481–484 (2009).
4. Abatzoglou, J. T. & Williams, A. P. Impact of anthropogenic climate change on wildfire across western US forests. *Proc. Natl Acad. Sci. USA* **113**, 11770–11775 (2016).
5. Westerling, A. L., Hidalgo, H. G., Cayan, D. R. & Swetnam, T. W. Warming and earlier spring increase Western U.S. forest wildfire activity. *Science* **313**, 940–943 (2006).
6. Hudson, P. K. et al. Biomass-burning particle measurements: characteristic composition and chemical processing. *J. Geophys. Res. Atmos.* **109**, D23S27 (2004).
7. Park, R. J., Jacob, D. J. & Logan, J. A. Fire and biofuel contributions to annual mean aerosol mass concentrations in the United States. *Atmos. Environ.* **41**, 7389–7400 (2007).
8. Edwards, D. P. et al. Satellite-observed pollution from Southern Hemisphere biomass burning. *J. Geophys. Res.* **111**, D14312 (2006).
9. Wotawa, G. & Trainer, M. The influence of Canadian forest fires on pollutant concentrations in the United States. *Science* **288**, 324–328 (2000).
10. Andreae, M. O., Andreae, T. W., Ferek, R. J. & Raemdonck, H. Long-range transport of soot carbon in the marine atmosphere. *Sci. Total Environ.* **36**, 73–80 (1984).
11. Zuidema, P. et al. The Ascension Island boundary layer in the remote Southeast Atlantic is often smoky. *Geophys. Res. Lett.* **45**, 4456–4465 (2018).
12. Dahlkötter, F. et al. The Pagami Creek smoke plume after long-range transport to the upper troposphere over Europe—aerosol properties and black carbon mixing state. *Atmos. Chem. Phys.* **14**, 6111–6137 (2014).
13. Ditas, J. et al. Strong impact of wildfires on the abundance and aging of black carbon in the lowermost stratosphere. *Proc. Natl Acad. Sci. USA* **115**, e11595–e11603 (2018).
14. Reddington, C. L. et al. The Global Aerosol Synthesis and Science Project (GASSP): measurements and modeling to reduce uncertainty. *Bull. Am. Meteorol. Soc.* **98**, 1857–1877 (2017).
15. Myhre, G. et al. Radiative forcing of the direct aerosol effect from AeroCom Phase II simulations. *Atmos. Chem. Phys.* **13**, 1853–1877 (2013).
16. Shi, Y. et al. A critical examination of spatial biases between MODIS and MISR aerosol products—application for potential AERONET deployment. *Atmos. Meas. Techn.* **4**, 2823–2836 (2011).
17. Watson-Parris, D. et al. On the Limits of CALIOP for constraining modeled free tropospheric aerosol. *Geophys. Res. Lett.* **45**, 9260–9266 (2018).
18. Thomson, D. S., Schein, M. E. & Murphy, D. M. Particle analysis by laser mass spectrometry WB-57F instrument overview. *Aerosol Sci. Technol.* **33**, 153–169 (2000).
19. Cziczo, D. J., Thomson, D. S., Thompson, T. L., DeMott, P. J. & Murphy, D. M. Particle analysis by laser mass spectrometry (PALMS) studies of ice nuclei and other low number density particles. *Int. J. Mass Spectrom.* **258**, 21–29 (2006).
20. Murphy, D. M. The design of single particle laser mass spectrometers. *Mass Spectrom. Rev.* **26**, 150–165 (2007).
21. Froyd, K. D. et al. A new method to quantify mineral dust and other aerosol species from aircraft platforms using single-particle mass spectrometry. *Atmos. Meas. Techn.* **12**, 6209–6239 (2019).
22. Brock, C. A. et al. Particle characteristics following cloud-modified transport from Asia to North America. *J. Geophys. Res.* **109**, D23S26 (2004).
23. Sofiev, M., Ermakova, T. & Vankevich, R. Evaluation of the smoke-injection height from wild-land fires using remote-sensing data. *Atmos. Chem. Phys.* **12**, 1995–2006 (2012).
24. Val Martin, M., Kahn, R. & Tosca, M. A global analysis of wildfire smoke injection heights derived from space-based multi-angle imaging. *Remote Sens.* **10**, 1609 (2018).
25. Reid, J. S. et al. A review of biomass burning emissions part II: intensive physical properties of biomass burning particles. *Atmos. Chem. Phys.* **5**, 799–825 (2005).
26. Li, J., Pósfai, M., Hobbs, P. V. & Buseck, P. R. Individual aerosol particles from biomass burning in southern Africa: 2, compositions and aging of inorganic particles. *J. Geophys. Res. Atmos.* **108**, 8484 (2003).
27. Chin, M. et al. Tropospheric aerosol optical thickness from the GOCART model and comparisons with satellite and sun photometer measurements. *J. Atmos. Sci.* **59**, 461–483 (2002).
28. Colarco, P., da Silva, A., Chin, M. & Diehl, T. Online simulations of global aerosol distributions in the NASA GEOS-4 model and comparisons to satellite and ground-based aerosol optical depth. *J. Geophys. Res.* **115**, D14207 (2010).
29. Bian, H. et al. Source attributions of pollution to the Western Arctic during the NASA ARCTAS field campaign. *Atmos. Chem. Phys.* **13**, 4707–4721 (2013).
30. Darmenov, A. & da Silva, A. M. *The Quick Fire Emissions Dataset (QFED) – Documentation of Versions 2.1, 2.2 and 2.4* Technical Report Series on Global Modeling and Data Assimilation No. 32 (NASA, 2015).
31. Bian, Q. et al. Secondary organic aerosol formation in biomass-burning plumes: theoretical analysis of lab studies and ambient plumes. *Atmos. Chem. Phys.* **17**, 5459–5475 (2017).
32. Petrenko, M. et al. The use of satellite-measured aerosol optical depth to constrain biomass burning emissions source strength in the global model GOCART. *J. Geophys. Res. Atmos.* **117**, D18212 (2012).

33. Pan, X. et al. Six global biomass burning emission datasets: intercomparison and application in one global aerosol model. *Atmos. Chem. Phys.* **20**, 969–994 (2020).
34. Schwarz, J. P. et al. Global-scale seasonally resolved black carbon vertical profiles over the Pacific. *Geophys. Res. Lett.* **40**, 5542–5547 (2013).
35. Yu, P. et al. Efficient in-cloud removal of aerosols by deep convection. *Geophys. Res. Lett.* **46**, 1061–1069 (2019).
36. Lund, M. T. et al. Short black carbon lifetime inferred from a global set of aircraft observations. *npj Clim. Atmos. Sci.* **1**, 31 (2018).
37. Toth, T. D. et al. Minimum aerosol layer detection sensitivities and their subsequent impacts on aerosol optical thickness retrievals in CALIPSO level 2 data products. *Atmos. Meas. Tech.* **11**, 499–514 (2018).
38. Samset, B. H. & Myhre, G. Climate response to externally mixed black carbon as a function of altitude. *J. Geophys. Res. Atmos.* **120**, 2913–2927 (2015).
39. Tegen, I. & Heinold, B. Large-scale modeling of absorbing aerosols and their semi-direct effects. *Atmosphere* **9**, 380 (2018).
40. Mallet, M. et al. Simulation of the transport, vertical distribution, optical properties and radiative impact of smoke aerosols with the ALADIN regional climate model during the ORACLES-2016 and LASIC experiments. *Atmos. Chem. Phys.* **19**, 4963–4990 (2019).
41. Toon, O. B. et al. Planning, implementation, and scientific goals of the Studies of Emissions and Atmospheric Composition, Clouds and Climate Coupling by Regional Surveys (SEAC 4 RS) field mission. *J. Geophys. Res. Atmos.* **121**, 4967–5009 (2016).

Methods

Aerosol sampling during ATom. The NASA ATom mission consisted of four series of seasonal flights from 2016 to 2018 that spanned the region between ~86° S and ~82° N over the remote Pacific and Atlantic Ocean basins. Flights consisted of six to ten altitude profiles from ~0.18 to 12 km, with ~5–15 min spent at the bottom and top of each profile. An extensive payload characterized both gas-phase and aerosol species (https://daac.ornl.gov/ATOM/guides/ATom_merge.html, accessed January 2020). The flight tracks for each seasonal series of flights, and its corresponding months, are shown in Supplementary Fig. 1. One of the main goals of ATom was to provide extensive constraints on both satellite measurements and global models that simulate atmospheric chemistry and climate.

In this work, we consider all of the ATom measurements as remote except for take-off ascents from cities, final approaches, missed approaches and low passes over continental landmasses. We chose not to filter out biomass burning plumes transported to the remote troposphere, such as air off the west coast of Africa with high biomass burning number fractions (Fig. 1a). If biomass burning plumes exist in the ATom dataset, however, we consider these as being in the remote troposphere for they are hundreds to thousands of kilometres from the nearest fire emissions. According to back-trajectory analyses, 99.6% of the ATom sampling periods had not encountered a fire in the previous 3 d.

Detailed descriptions of the aerosol sampling and sizing instruments[42] and PALMS[43] as operated during ATom have been published. The aerosol-sizing instruments consisted of one or two nucleation-mode aerosol-size spectrometers (NMASS)[44], the Droplet Measurement Technologies Ultra High Sensitivity Aerosol Spectrometer (UHSAS)[45] and the TSI Laser Aerosol Spectrometer (LAS), which were merged together into one size distribution[42]. The NMASS, UHSAS, LAS and PALMS spectrometers sampled air from outside the aircraft via the University of Hawaii (UH) inlet, now operated by the NASA Langley Aerosol Research Group (LARGE).

The UH/LARGE inlet was chosen specifically because it has been shown to transmit supermicrometre particles efficiently: particles ≥3.2 µm were sampled from the inlet with >50% efficiency at 12 km, and particles ≥5.0 µm were sampled with ~50% efficiency at lower altitudes[46]. Tubing losses for the supermicrometre particles were taken into consideration[47], with losses <30% for 1-µm particles and <80% for 5-µm particles. A virtual impactor, based on the design of Loo and Cork[48], was employed upstream of the PALMS instrument to enhance large-particle concentrations. The enhancement of large particles for PALMS improves particle statistics but does not affect concentrations, because PALMS data are scaled to match independent measurements of the size distributions as described below.

Particles passed through Nafion dryers before entering the aerosol-sizing instruments. The flow to PALMS was not actively dried, but the final 5 cm of tubing upstream of the PALMS aerosol focusing inlet was heated to 35 °C. Heating the line reduced the relative humidity in the aerosol inlet to <40%.

We exclude in-cloud data from the results in this work. Sea-salt particles in the marine boundary layer can be deposited on the walls of an aircraft inlet[49]. When passing through a cloud, droplets and/or ice particles will dislodge salt from the inlet wall or ablate off metallic particles, and these artefacts are measured by PALMS and the aerosol-sizing instruments[50,51].

PALMS. The PALMS instrument has been described in detail previously[18–21]. Briefly, a pressure-controlled (26-torr), six-stage aerodynamic lens focuses ambient particles into a collimated aerosol beam. The beam enters the ion source region (~0.2 torr), where a 405-nm, continuous-wave laser detects particles optically. Particle detection triggers a pulsed, 193-nm excimer laser that both vaporizes (ablates) particles and ionizes its constituents. Ions are extracted from the ion source region and sent through a time-of-flight mass spectrometer. Over 90% of optically detected particles produce mass spectra, largely due to the prompt firing of the excimer laser (400 ns) and the proximity of the trigger beam to the excimer laser pulse (100 µm). One positive- or negative-ion mass spectrum is produced per particle. The lower size limit for PALMS is not a fixed number due to variations in the aerosol inlet alignment, laser power and optical noise in the source region. Generally, the detection efficiency decreases with decreasing particle diameter, especially below ~150 nm, where PALMS can be statistically limited under low aerosol loadings; however, the PALMS detection efficiency does not affect biomass burning quantification under the assumptions described below.

The 405-nm laser is beam-split, adding an additional laser beam to the source region. The split beams are a known distance apart (33.1 mm), orthogonal to the focused aerosol stream. Optical detection by both lasers allows for a precise calculation of velocity from the time of flight between the two lasers. Particle velocity was calibrated to vacuum aerodynamic diameters using polystyrene latex spheres before and after each ATom deployment.

Particles are classified into eight different composition types based on their mass spectra, including sulfate-organic-nitrate, biomass burning, mineral dust/metallic, sea salt, elemental carbon (BC without thick organic coatings), meteoric particles, oil combustion from shipping emissions, and K-rich salt particles[21]. Particles that do not fit these particle types are placed into a ninth class, 'Other'. Spectral signatures that define particle types are often minor constituents. For example, meteoric particles, classified by the meteoric metals Fe, Ni and Mg, are mostly sulfuric acid by mass. Generally, minor or accumulated constituents will not obscure the spectral signatures. For example, mineral dust coated by small amounts of sulfate, organics and nitrate will still be classified as mineral dust/metallic. One exception is the elemental carbon particle type—the spectral signatures of the elemental carbon type are often obscured organic and sulfate signatures. During ATom, the PALMS elemental carbon particle type was not detected in high number fractions ($\ll 1\%$), suggesting that most of the black carbon was coated with organic material and/or sulfate. In addition to the empirical particle classifications, a hierarchical cluster analysis[52] was performed for all of the ATom mass spectra combined. The cluster analysis is not used directly to classify particles, but is useful in reducing hundreds of thousands of spectra down to hundreds of clusters. Clusters can then be hand-checked and, if misclassified, can be manually added to, or removed from, composition types.

Biomass burning aerosol identification using PALMS. The PALMS biomass burning index is a semi-empirical biomass burning classification originally developed by Hudson et al.[6] and modified here to further improve identification accuracy. It operates by multiplying the relative peak areas of carbon (A12) by the square of a modified potassium signal (MA39), and normalizing that product. By squaring MA39, more weight is given to potassium than carbon in the biomass burning index. The modified potassium area has maintained its original functional form[6], but the empirical coefficients change slightly from mission to mission. The potassium peak area is modified to filter out other particle types that could contain trace amounts of potassium, including sea salt, minerals and meteoric material, industrial sources, oil combustion from shipping activity, and K-rich salt particles.[6] The biomass burning index found >90% biomass burning particles in both fresh (~2 h) and aged (~7–10 d) biomass burning plumes identified by gas-phase tracers[6], indicating that MA39 is a conserved biomass burning tracer over atmospherically relevant aerosol lifetimes. PALMS is exquisitely sensitive to alkali metals, such that potassium is reliably detected in PALMS at $\ll 0.1\%$ by mass[53]. Bulk aerosol potassium measurements are not always selective for biomass burning aerosol due to high detection limits; furthermore, potassium mass is not linearly correlated with biomass burning mass because it may be more prevalent under flaming conditions[54]. PALMS, however, checks only for the presence of non-sea salt/dust/industrial potassium. Thus, single-particle selectivity combined with high potassium sensitivity allows for PALMS to identify biomass burning particles with high accuracy.

Biomass burning quantification using aerosol-sizing instruments and PALMS. PALMS natively measures fractional, rather than absolute, abundances. The latter is difficult for PALMS to measure per se due to substantial biases in sampling efficiencies; however, quantitative information can be derived by merging PALMS fractional data with independently measured quantitative size distributions. The methodology and limitations have been detailed by Froyd et al.[21]. Briefly, PALMS aerodynamic diameters are converted to geometric diameters using composition-dependent densities and dynamic shape factors. Geometric diameters are then matched to aerosol size distribution data. PALMS has size-dependent detection biases, but PALMS ionizes all major particle types with similar efficiency[55]. Thus, the number fraction of each composition type can be multiplied by the concentration in an aerosol size distribution bin, providing it is sufficiently narrow. An inherent assumption is that particle composition is relatively homogeneous within a single size bin. This results in a composition-resolved size distribution. The distribution can be a number, surface area or volume size distribution, with PALMS providing larger data coverages for the latter two. Biomass burning aerosol mass concentrations were calculated on a 3-min time basis using the method of Froyd et al.[21]. In this work, we used four size bins (0.10–0.25, 0.25–0.63, 0.63–1.13 and 1.13–5.03 µm). The relative errors for biomass burning number fractions and mass concentrations are primarily driven by sampling statistics and are a function of total concentration and the number of particles sampled in a 3-min window. The estimated statistical errors for a 3-min window are ~30% at a mass concentration of 0.01 µg m^{-3}, and decrease to ~10% at 0.1 µg m^{-3} (ref. [21]).

Biomass burning aerosol in the GEOS model incorporating the GOCART module. GEOS is a global Earth system model that simulates atmospheric circulation and composition, ocean circulation, biogeochemistry and land–surface processes[56]. The GOCART module simulates aerosol sources, sinks, transport and transformation in GEOS[27–29]. The major tropospheric aerosol compositions are represented, including BC, organic carbon, sulfate, nitrate, dust and sea salt. The module also includes gas- and liquid-phase reactions that convert sulfate precursors (SO_2 and dimethyl sulfide) into sulfate aerosol. Aerosols are treated as externally mixed and do not interact with each other. For the ATom comparisons, GEOS/GOCART was run at a global ~50-km horizontal resolution with 72 vertical pressure layers from the surface up to 0.01 mbar (~85 km). The dynamical time step was 450 s. The model was run in 'replay mode', which resets the model dynamical state every 6 h to a balanced state provided by the Modern-era Reanalysis for Research and Applications v.2 atmospheric reanalysis. A 2-yr simulation was conducted from the beginning of 2016 to cover all of the ATom missions. The first half of 2016 was used as a spin-up period.

Biomass burning aerosol was tagged by using an emissions on–minus–off approach. Emissions of biomass burning organic carbon, BC, ammonia and SO_2 are derived from QFED v.2.4 (ref. [30]). The QFED emissions are top-down, using MODIS fire radiative power (FRP) to derive the amount of dry mass burned. Emission factors relating to FRP are calibrated against the global monthly mean emissions of the Global Fire Emissions Database (GFED) v.2. For aerosol species, QFED emissions are further calibrated with biome-specific enhancing factors, which are based on constraints of model AOD to MODIS AOD in four biomes. Injection heights are considered to be homogeneously distributed throughout the GEOS boundary layer; this is a reasonable estimate, as it has been shown that >80% of plume heights are within the boundary layer[23,24]. In these runs, 80% of the BC and 50% of the organic carbon was emitted as hydrophobic, with the remainder being hydrophilic. BC and organic carbon 'age' in the model, converting from hydrophobic to hydrophilic with an e-folding time of 2.5 d. Aerosol is removed by dry deposition, wet removal and convective scavenging. Under normal operation, only hydrophilic aerosol is subject to wet removal and convective scavenging following the treatment of Liu et al.[57].

GEOS/GOCART AOD was calculated from dry aerosol mass, and requires composition-dependent assumption of the refractive indices, size distributions and hygroscopic properties of aerosols. Log-normal size distributions and hygroscopic growth factors for GOCART aerosol can be found in Chin et al.[27]. Optical properties in this study are as described in Randles et al.[58]. Aerosols are radiatively coupled to the atmospheric general circulation model via the Chou–Suarez CLDRAD radiation code[59]. This model accounts for absorption by O_3, CO_2, O_2, H_2O and aerosols. It also accounts for scattering by clouds, aerosols and gases. The solar spectrum (0.2–10 μm) is divided into eight bands in the ultraviolet and visible range, and an additional three bands in the near-infrared. AOD, single-scattering albedo and asymmetry factors were calculated for the radiative transfer simulation. The radiative transfer solution can be recycled with various experimental atmospheric conditions, such as clean air (no aerosols) and clear sky (no clouds). In this work, the all-sky instantaneous direct radiative effect was calculated as the net change in radiation flux at the top of the atmosphere due to all aerosols.

For model–measurement comparisons, a virtual aircraft was flown through the model domain along the same spatiotemporal coordinates as the observations. A simple linear interpolation was applied in both space and time and thus, as the model aircraft flew from one grid cell to the next, the values changed continuously.

Model–measurement comparisons and sensitivity tests. To investigate the discrepancies between PALMS biomass burning organic-only mass with GEOS/GOCART biomass burning mass, 12 sensitivity tests were run; these tests were run for the summer and winter months only. The parameter-space explored included different combinations of emissions datasets, hydrophobic-to-hydrophilic ageing, wet removal in cold-cloud ($T < 258$ K) and removal of hydrophobic aerosol due to impaction in large-scale and convective clouds (Supplementary Table 2). To assess the capacity of GEOS/GOCART in reproducing the PALMS biomass burning observations, we calculated both the mean log bias of the model and centred root mean squared error (CRMSE). The mean log bias was calculated as follows:

$$\text{Mean log bias} = \frac{1}{N}\sum_{i}^{N}[\log(M_i) - \log(O_i)] \quad (1)$$

where N is the number of observations, M_i is the model value for point i and O_i is the observed value for point i. The mean log bias is useful for measurements with a high dynamic range, because it gives equal weight to low and high values. Zero values, while rare, are possible in either dataset. These values are ignored in the comparison. The mean log bias is easy to interpret without having to normalize the values: a mean log bias of ±0.3 means that the model is biased, on average, by a factor of two ($\sim 10^{0.3} = 2$). Similarly, a model with mean log bias of ±1 means that the model is biased by an order of magnitude. CRMSE is calculated as the square root of the mean squared difference in model–observation pairings. By centring the RMSE, we remove any contribution from the mean bias. Since large errors are weighted heavily in CRMSE, we determined CRMSLE instead:

$$\text{CRMSLE} = \sqrt{\frac{1}{N}\sum_{i}^{N}[(\log(M_i) - \log(\bar{M})) - (\log(O_i) - \log(\bar{O}))]^2}. \quad (2)$$

If the differences in the model–observation pairings are normally distributed for N data points, then CRMSE is analogous to the s.d. of the errors. Thus, while the mean log bias indicates whether data are skewed on average, CRMSLE indicates the width of the errors around that skewed average. Together, the two values provide a complete description of the errors analogous to the means and s.d. of a normally distributed dataset. Mean log bias and CRMSLE were calculated for each ocean basin separately, to minimize potential biases from emission and transport.

Compared to all other regions, the model underestimates biomass burning abundance in the Pacific Northern Hemisphere mid-latitudes (Fig. 3), which may be due to either excessive wet removal, low emissions or transport errors. This was taken into account when scoring model runs, giving credence to mean log bias scores that were slightly negative in the Pacific as opposed to values that were closer to zero.

Trace organic gas analyser (TOGA). Acetonitrile (CH_3CN) and hydrogen cyanide (HCN) were measured by TOGA. TOGA is a fast online gas chromatography/mass spectrometry technique that analysed 35-s integrated samples every 2 min during ATom. It has been described in detail previously[60,61]. Briefly, TOGA was developed specifically for aircraft use to provide a wide range of volatile organic compound (VOC) measurements in one instrument, including the identification and quantification of non-methane hydrocarbons, oxygenated VOCs (including formaldehyde, other aldehydes, ketones and alcohols), nitriles (HCN and CH_3CN) and halogenated VOCs. Limits of detection range from 20 ppt (formaldehyde and methanol) to <1 ppt (for example, toluene).

TOGA uses a pre-concentration system consisting of a water trap, an enrichment trap and a cryofocusion trap in series. Trap temperatures are cycled rapidly, using cryogenically cooled N_2 gas for cooling and resistive wires for heating. The trap cooling system is efficient, with cryogenic cooling attained in ~30 s to a precision of ±0.5 °C over the range 100 to −135 °C.

The TOGA GC is a custom-made, low thermal mass unit that attains rapid heating and cooling, as well as high precision, for good run-to-run reproducibility. When combined with a 200-$ft^3\,min^{-1}$ fan (below the oven), the GC exhibits rates of 10 °C s^{-1} heating and −5 °C s^{-1} cooling. A Restek MXT-624, 6-m, 0.18-mm identity column is used for chromatography. Helium is used as a carrier gas.

TOGA uses a shock-mounted Agilent Technologies 5973N quadrupole mass spectrometer system. A custom oil-free, three-stage vacuum system has been implemented, to both increase sensitivity and eliminate the possibility of contamination through oil back-diffusion. Selected ion monitoring is used to quantify individual compounds. High-speed electronics allows the simultaneous measurement of peaks with <1-s peak width. Calibration and blanks are achieved during flight using an onboard zero air/dynamic dilution calibration system coupled with onboard calibration gas mixtures.

Fire influence. Back trajectories were used to estimate the probability of, and time since, fire influence for each of the ATom flights. A cluster of 245 back trajectories was initialized every minute along the flight tracks using the Traj3d model[62,63] with National Centers for Environmental Prediction meteorology (0.5° × 0.5° resolution). Back trajectories were run for 30 d. Fire influence was estimated based on the coincidence in time and location of the back trajectories with active fires based on MODIS FRP (Collection 6), Visible Infrared Imaging Radiometer Suite (VIIRS) 375-m FRP[64] and GFED v2. Fire plume heights for MODIS and VIIRS were calculated based on FRP[23], and for GFED were assumed to be confined to the boundary layer. A trajectory was considered to be influenced by a fire if it coincided with a MODIS, VIIRS or GFED fire location and time and was below the altitude of the fire plume height. The number of days since most recent fire influence for each flight minute were calculated by averaging the time since the most recent fire influence of all trajectories in each cluster.

Data availability

Data are publically available at https://daac.ornl.gov/ATOM/guides/ATom_merge.html and https://esrl.noaa.gov/csd/projects/atom/data.php.

Code availability

GEOS is an open-source model, and the code is available at https://gmao.gsfc.nasa.gov/GEOS_systems/.

References

42. Brock, C. A. et al. Aerosol size distributions during the Atmospheric Tomography Mission (ATom): methods, uncertainties, and data products. *Atmos. Meas. Tech.* **12**, 3081–3099 (2019).
43. Murphy, D. M. et al. The distribution of sea-salt aerosol in the global troposphere. *Atmos. Chem. Phys.* **19**, 4093–4104 (2019).
44. Williamson, C. et al. Fast time response measurements of particle size distributions in the 3–60 nm size range with the nucleation mode aerosol size spectrometer. *Atmos. Meas. Tech.* **11**, 3491–3509 (2018).
45. Kupc, A., Williamson, C., Wagner, N. L., Richardson, M. & Brock, C. A. Modification, calibration, and performance of the Ultra-High Sensitivity Aerosol Spectrometer for particle size distribution and volatility measurements during the Atmospheric Tomography Mission (ATom) airborne campaign. *Atmos. Meas. Tech.* **11**, 369–383 (2018).
46. McNaughton, C. S. et al. Results from the DC-8 Inlet Characterization Experiment (DICE): airborne versus surface sampling of mineral dust and sea salt aerosols. *Aerosol Sci. Technol.* **41**, 136–159 (2007).
47. Brockmann, J. E. in *Aerosol Measurement* (eds Kulkarni, P. et al.) Ch. 6 (John Wiley & Sons, 2011).
48. Loo, B. W. & Cork, C. P. Development of high efficiency virtual impactors. *Aerosol Sci. Technol.* **9**, 167–176 (1988).
49. Huebert, B. J., Lee, G. & Warren, W. L. Airborne aerosol inlet passing efficiency measurement. *J. Geophys. Res.* **95**, 16369–16381 (1990).
50. Weber, R. J. et al. Spurious aerosol measurements when sampling from aircraft in the vicinity of clouds. *J. Geophys. Res. Atmos.* **103**, 28337–28346 (1998).

51. Murphy, D. M. et al. Particle generation and resuspension in aircraft inlets when flying in clouds. *Aerosol Sci. Technol.* **38**, 401–409 (2004).
52. Murphy, D. M., Middlebrook, A. M. & Warshawsky, M. Cluster analysis of data from the Particle Analysis by Laser Mass Spectrometry (PALMS) instrument. *Aerosol Sci. Technol.* **37**, 382–391 (2003).
53. Cziczo, D. J., Thomson, D. S. & Murphy, D. M. Ablation, flux, and atmospheric implications of meteors inferred from stratospheric aerosol. *Science* **291**, 1772–1775 (2001).
54. Sullivan, A. P. et al. Biomass burning markers and residential burning in the WINTER aircraft campaign. *J. Geophys. Res. Atmos.* **124**, 1846–1861 (2019).
55. Cziczo, D. J. et al. Observations of organic species and atmospheric ice formation. *Geophys. Res. Lett.* **31**, L12116 (2004).
56. Rienecker, M. M. et al. *The GEOS-5 Data Assimilation System: Documentation of Versions 5.0. 1, 5.1. 0, and 5.2. 0* Technical Report Series on Global Modeling and Data Assimilation No. 27 (NASA, 2008).
57. Liu, H., Jacob, D. J., Bey, I. & Yantosca, R. M. Constraints from ^{210}Pb and ^{7}Be on wet deposition and transport in a global three-dimensional chemical tracer model driven by assimilated meteorological fields. *J. Geophys. Res. Atmos.* **106**, 12109–12128 (2001).
58. Randles, C. A. et al. The MERRA-2 aerosol reanalysis, 1980 Onward. Part I: system description and data assimilation evaluation. *J. Clim.* **30**, 6823–6850 (2017).
59. Chou, M. & Suarez, M. J. *A Solar Radiation Parameterization for Atmospheric Studies* Technical Report Series on Global Modeling and Data Assimilation No. 15 (NASA, 1999).
60. Apel, E. C. et al. Upper tropospheric ozone production from lightning NO_x-impacted convection: smoke ingestion case study from the DC3 campaign. *J. Geophys. Res. Atmos.* **120**, 2505–2523 (2015).
61. Wang, S. et al. Atmospheric acetaldehyde: importance of air–sea exchange and a missing source in the remote troposphere. *Geophys. Res. Lett.* **46**, 5601–5613 (2019).
62. Bowman, K. P. Large-scale isentropic mixing properties of the Antarctic polar vortex from analyzed winds. *J. Geophys. Res.* **98**, 23013 (1993).
63. Bowman, K. P. & Carrie, G. D. The mean-meridional transport circulation of the troposphere in an idealized GCM. *J. Atmos. Sci.* **59**, 1502–1514 (2002).
64. Schroeder, W., Oliva, P., Giglio, L. & Csiszar, I. A. The new VIIRS 375 m active fire detection data product: algorithm description and initial assessment. *Remote Sens. Environ.* **143**, 85–96 (2014).

Acknowledgements

The mission as a whole was supported by NASA's Earth System Science Pathfinder Program EVS-2 funding. Participation in ATom Mission flights by G.P.S., K.D.F., C.W., C.A.B. and D.M.M. was supported by NOAA climate funding (no. NNH15AB12I). A.K. was supported by the Austrian Science Fund's Erwin Schrodinger Fellowship (no. J-3613). R.S.H., A.J.H. and E.C.A. received support from the National Center for Atmospheric Research, which is a major facility sponsored by the NSF under Cooperative Agreement no. 1852977.

Author contributions

G.P.S., K.D.F. and D.M.M. provided PALMS data. H.B., M.C. and P.R.C. provided GEOS/GOCART results. A.K., C.W. and C.A.B. provided size distribution data. E.R. provided back-trajectory results. R.S.H., A.J.H. and E.C.A. provided TOGA data. G.P.S. wrote the paper with assistance from all authors.

Competing interests

The authors declare no competing interests.

Additional information

Supplementary information is available for this paper at https://doi.org/10.1038/s41561-020-0586-1.

Correspondence and requests for materials should be addressed to G.P.S.

Peer review information Primary Handling Editors: Clare Davis; Xujia Jiang.

Reprints and permissions information is available at www.nature.com/reprints.